Updated Low-temperature Gas Opacities with ÆSOPUS 2.0

Paola Marigo[1] , Bernhard Aringer[2] , Léo Girardi[3] , and Alessandro Bressan[4]
[1] Department of Physics and Astronomy G. Galilei, University of Padova, Vicolo dell'Osservatorio 3, I-35122, Padova, Italy; paola.marigo@unipd.it
[2] Department of Astrophysics, University of Vienna, Türkenschanzstrasse 17, A-1180 Vienna, Austria
[3] INAF–Osservatorio Astronomico di Padova Vicolo dell'Osservatorio 5, I-35122 Padova, Italy
[4] SISSA, via Bonomea 265, I-34136 Trieste, Italy

Abstract

This work introduces new low-temperature gas opacities in the range $3.2 \lesssim \log(T/\mathrm{K}) \lesssim 4.5$ computed with the ÆSOPUS code under the assumption of thermodynamic equilibrium. In comparison to the previous version, ÆSOPUS 1.0, we updated and expanded molecular absorption to include 80 species, mostly using the recommended line lists currently available from the ExoMol and HITRAN databases. Furthermore, in light of a recent study, we revised the H^- photodetachment cross section, added the free–free absorption of other negative ions of atoms and molecules, and updated the collision-induced absorption due to H_2/H_2, H_2/H, H_2/He, and H/He pairs. Using the new input physics, we computed tables of Rosseland mean opacities for several scaled-solar chemical compositions, including Magg et al.'s most recent one, as well as α-enhanced mixtures. The differences in opacity between the new ÆSOPUS 2.0 and the original ÆSOPUS 1.0 versions, as well as other sets of calculations, are discussed. The new opacities are released to the community via a dedicated webpage that includes both precomputed tables for widely used chemical compositions and a web interface for calculating opacities on the fly for any abundance distribution.

1. Introduction

Low-temperature gas opacities in the approximate temperature range $1500 \lesssim T/\mathrm{K} \lesssim 10{,}000$ play a pivotal role in a variety of astrophysical applications. The continuous absorption of the negative hydrogen ion H^-, for example, is one of the most important opacity sources in our Sun's atmosphere, the strength of which is also dependent on the availability of free electrons provided by elements with relatively low ionization potentials, primarily Mg, Si, Fe, Al, C, and Ca. Molecular opacities dominate the atmospheres of cool stars with temperatures $T < 4500$ K (pre-main-sequence stars, main-sequence red dwarfs, red giants, and supergiants). Following the discovery of thousands of exoplanets by space missions such as Kepler and Corot, the demand for molecular opacities has grown tremendously in recent decades (Tennyson & Yurchenko 2012; Chubb et al. 2021; Grimm et al. 2021). Furthermore, the advent of high-resolution and large spectroscopic surveys has revealed a wide range of chemical patterns at the photospheres of stars (see Jofré et al. 2019, for a thorough review), which must be addressed properly by theory with stellar models that include consistent chemical composition and opacity.

For many years, the Wichita State University group (e.g., Alexander & Ferguson 1994; Ferguson et al. 2005) has been the historical supplier of low-temperature opacities. Typically, these authors provided opacity tables for scaled-solar or α-enhanced mixtures primarily designed for stellar structure computations. Other groups have produced low-temperature opacities suitable for brown dwarfs and planetary atmospheres (Sharp & Burrows 2007; Chubb et al. 2021; Grimm et al. 2021), protoplanetary disks (Semenov et al. 2003), primordial matter (Harris et al. 2004; Mayer & Duschl 2005), and carbon- and nitrogen-enriched asymptotic giant branch (AGB) stars (Lederer & Aringer 2009).

In 2009, Marigo & Aringer developed the ÆSOPUS code, which solves the equation of state for over 800 chemical species (300 atoms/ions and 500 molecules) and calculates the Rosseland mean opacities for any combination of abundances assuming thermodynamic equilibrium. The primary goal of that work was to greatly expand public access to Rosseland mean opacity data in the low-temperature regime. We created a web interface (http://stev.oapd.inaf.it/aesopus) that allows users to compute and quickly retrieve Rosseland mean opacity tables based on their specific needs, with complete control over the chemical composition of the gas (individual abundances can be set for 92 atomic species, ranging from hydrogen to uranium).

A distinguishing quality of ÆSOPUS is its quick performance, which is made possible by an optimized application of the opacity sampling (OS) method. The typical computation time for one table at fixed chemical composition arranged with the default parameter grid (temperature T and $R = \rho/(T/10^6\,\mathrm{K})^3$), i.e., containing $N_T \times N_R = 67 \times 19 = 1273$ opacity values, is less than 50 s with a 2.0 GHz processor. Thanks to this property, we could make ÆSOPUS available online through a web interface that generates opacity tables in real time with maximum flexibility and minimal computational cost. Furthermore, one of the interface's most useful features is the ability to generate a large database of opacity tables with varying C, N, and O abundances. This is critical for accurately modeling the atmospheric layers of AGB stars, the surface composition of which is frequently altered by mixing episodes (third dredge-up), and nucleosynthesis in the convective envelope (hot-bottom burning), as well as massive and supergiant stars.

The ÆSOPUS tool has being used by several groups to model, e.g., AGB stars (Karakas & Lugaro 2016; Ventura et al. 2018), super-AGB stars (Gil-Pons et al. 2018), long-period variables (Trabucchi et al. 2021), supernova light curves (Takei & Shigeyama 2020), and white dwarfs (Althaus et al. 2010). An extended grid of ÆSOPUS tables with varying CNO abundances is currently implemented in the MESA code (Paxton et al. 2011).

In this paper, we present AESOPUS 2.0, a renewed version of our chemistry and opacity code. We have significantly updated and expanded its ingredients, primarily in relation to the opacity sources, partition functions, and computation-speeding strategies. In addition, we have included the most recent solar chemical compositions published in the literature (e.g., Asplund et al. 2021; Magg et al. 2022). We generated a large number of Rosseland mean opacity tables for several values of metallicity and hydrogen abundance, solar compositions, and α-enhanced mixtures. They can be found at http://stev.oapd.inaf.it/aesopus_2.0/tables; a copy of these files have also been deposited to Zenodo, https://doi.org/10.5281/zenodo.7219874. The ÆSOPUS web interface for Rosseland mean opacities on demand has also been refurbished.

The paper is structured as follows. Section 2 recaps the main ÆSOPUS ingredients and recalls the physical definition of the Rosseland mean opacity. Section 3 introduces the major updates and revisions implemented in the new version, ÆSOPUS 2.0, and discusses the optimization of the OS method. Section 4 presents and examines the results, with particular focus on Rosseland mean opacities computed for scaled-solar abundances. Section 5 explores the first tests of the new opacities in stellar models. Section 6 introduces the new opacity tables, accessible via a public repository, while Section 7 advertises the web interface for on-the-fly opacity computation. Finally, Section 8 concludes the paper.

2. Equation of State and Opacity in ÆSOPUS

For a detailed description of the ÆSOPUS code, see Marigo et al. (2009; initial version ÆSOPUS 1.0). Suffice it here to recall the basic ingredients. ÆSOPUS solves the equation of state for more than 800 species (about 300 atoms and ions and 500 molecules) in the gas phase under the assumption of an ideal gas in both thermodynamic and instantaneous chemical equilibrium. For all elements from C to Ni, we take into account ionization stages from I to V (up to VI for O and Ne), and for heavier atoms from Cu to U, we consider ionization stages from I to III. ÆSOPUS accounts for continuum opacity processes (Rayleigh scattering, Thomson scattering, bound–free absorption due to photoionization, free–free absorption, and collision-induced absorption, CIA) and line opacity processes (atomic bound–bound and molecular band absorption). For a description of the opacity sources in the current version of ÆSOPUS, referred to as ÆSOPUS 2.0, see Tables 1 and 2 below.

2.1. The Rosseland Mean Opacity

The solution to the radiation transfer equation greatly simplifies in a gas under conditions of local thermodynamic equilibrium, energy transport diffusion approximation, and spherical symmetry, such that the flux $F(r)$ at the radial coordinate r, with gas density ρ and temperature T, becomes

$$F(r) = -\frac{4\pi}{3}\frac{1}{\kappa_R(\rho, T)}\frac{\partial B(r, T)}{\partial r}, \qquad (1)$$

where $B(r, T)$ is the integral of the Planck function over frequency, and κ_R is a frequency-integrated average opacity known as the Rosseland mean opacity, which is calculated as follows.

For any given combination (ρ, T), we first compute the total monochromatic opacity cross section per unit mass (in cm^2 g^{-1}) by adding all of the contributions from true absorption and scattering,

$$\kappa(\nu) = \sum_j [\kappa_j^{abs}(\nu) + \kappa_j^{scatt}(\nu)] \qquad (2)$$

$$=\sum_j \frac{n_j}{\rho} [\sigma_j^{abs}(\nu)(1 - e^{-h\nu/k_B T}) + \sigma_j^{scatt}(\nu)], \qquad (3)$$

where n_j is the number density of particles of type j, $\sigma_j^{abs/scatt}(\nu)$ is the corresponding absorption/scattering monochromatic cross section (in cm^2), and the factor $(1 - e^{-h\nu/k_B T})$ accounts for stimulated emission.

Second, we integrate over frequency to obtain the Rosseland mean opacity, κ_R (in cm^2 g^{-1}),

$$\frac{1}{\kappa_R(\rho, T)} = \frac{\int_0^\infty \frac{1}{\kappa(\nu)}\frac{\partial B_\nu}{\partial T}d\nu}{\int_0^\infty \frac{\partial B_\nu}{\partial T}d\nu}, \qquad (4)$$

which is a harmonic weighted average, with weights equal to the temperature derivatives of the Planck distribution with respect to temperature, $\frac{\partial B_\nu}{\partial T}$.

For ease of use, Rosseland mean opacity tables are typically constructed as a function of the logarithm of the temperature T (in K units) and the logarithm of the R variable, which is defined as $R = \rho\, T_6^{-3}$ (with ρ in $g\,cm^{-3}$ and $T_6 = T/(10^6\,K)$). Employing the R parameter rather than density ρ or pressure P allows the opacity tables to cover rectangular regions of the (R, T) plane and provides a suitable format for smooth opacity interpolation. Our Rosseland mean opacity tables extend over the temperature range $3.2 \leqslant \log(T) \leqslant 4.5$ and the R interval $-1.0 \leqslant \log(R) \leqslant 8.0$.

3. Major Updates in ÆSOPUS 2.0

In this work, we expand and update a significant number of opacity sources (Tables 1 and 2) and thermodynamic data. In addition, we revise various partition functions for diatomic molecules taken from Barklem & Collet (2016) and the ExoMol database (Tennyson & Yurchenko 2012). Below, we only highlight the most significant changes in opacity that refer to the continuous absorption from the negative hydrogen ion, CIA, and molecular absorption. In addition to H^-, negative ion free–free opacity from other species is also included and/or revised (He^-, Li^-, C^-, N^-, O^-, Ne^-, Cl^-, H_2O^-, CO^-, and N_2^-).

3.1. Photodetachment of H^-

Since the pioneering work of Chandrasekhar & Breen (1946), continuous absorption from the negative hydrogen ion has been recognized as an important opacity source in the stellar atmospheres. John (1988) analytic fits to theoretical data

Table 1
Scattering and Absorption Processes

Process	Symbol	Reaction	References and Comments
Rayleigh	$\sigma_{\rm Ray}({\rm H_2})$	$\rm H_2 + h\nu \rightarrow H_2 + h\nu'$	Dalgarno & Williams (1962)
	$\sigma_{\rm Ray}({\rm H})$	$\rm H + h\nu \rightarrow H + h\nu'$	Gavrila (1967) using fit of Ferland (2000)
	$\sigma_{\rm Ray}({\rm He})$	$\rm He + h\nu \rightarrow He + h\nu'$	Dalgarno 1962
Thomson	${\rm Th}(e^-)$	$\rm e^- + h\nu \rightarrow e^- + h\nu'$	NIST (2018 CODATA recommended value)
Free–free	$\sigma_{\rm ff}({\rm H^-})$	$\rm H + e^- + h\nu \rightarrow H + e^-$	Bell & Berrington (1987) using fit of John (1988)
	$\sigma_{\rm ff}({\rm H})$	$\rm H^+ + e^- + h\nu \rightarrow H^+ + e^-$	Method as Kurucz (1970) based on Karzas & Latter (1961)
	$\sigma_{\rm ff}({\rm H_2^+})$	$\rm H^+ + H + h\nu \rightarrow H^+ + H$	Lebedev et al. (2003)
	$\sigma_{\rm ff}({\rm H_2^-})$	$\rm H_2 + e^- + h\nu \rightarrow H_2 + e^-$	John (1975)
	$\sigma_{\rm ff}({\rm H_3})$	$\rm H_3^+ + e^- + h\nu \rightarrow H_3^+ + e^-$	$\sigma_{\rm ff}({\rm H_3}) = \sigma_{\rm ff}({\rm H})$ (assumed)
	$\sigma_{\rm ff}({\rm He^-})$	$\rm He + e^- + h\nu \rightarrow He + e^-$	John (1994)
	$\sigma_{\rm ff}({\rm He})$	$\rm He^+ + e^- + h\nu \rightarrow He^+ + e^-$	$\sigma_{\rm ff}({\rm He}) = \sigma_{\rm ff}({\rm H})$ (assumed)
	$\sigma_{\rm ff}({\rm He^+})$	$\rm He^{++} + e^- + h\nu \rightarrow He^{++} + e^-$	$\sigma_{\rm ff}({\rm He^+}) = \sigma_{\rm ff}({\rm H})$ (assumed)
	$\sigma_{\rm ff}({\rm Li^-})$	$\rm Li + e^- + h\nu \rightarrow Li + e^-$	Ramsbottom & Bell (1996)
	$\sigma_{\rm ff}({\rm C^-})$	$\rm C + e^- + h\nu \rightarrow C + e^-$	Bell et al. (1988)
	$\sigma_{\rm ff}({\rm N^-})$	$\rm N + e^- + h\nu \rightarrow N + e^-$	Ramsbottom et al. (1992)
	$\sigma_{\rm ff}({\rm O^-})$	$\rm O + e^- + h\nu \rightarrow O + e^-$	John (1975)
	$\sigma_{\rm ff}({\rm Ne^-})$	$\rm Ne + e^- + h\nu \rightarrow Ne + e^-$	John (1996)
	$\sigma_{\rm ff}({\rm Cl^-})$	$\rm Cl + e^- + h\nu \rightarrow Cl + e^-$	John et al. (1975)
	$\sigma_{\rm ff}({\rm H_2O^-})$	$\rm H_2O + e^- + h\nu \rightarrow H_2O + e^-$	John (1975)
	$\sigma_{\rm ff}({\rm CO^-})$	$\rm CO + e^- + h\nu \rightarrow CO + e^-$	John (1975)
	$\sigma_{\rm ff}({\rm N_2^-})$	$\rm N_2 + e^- + h\nu \rightarrow N_2 + e^-$	John (1975)
Bound–free	$\sigma_{\rm bf}({\rm H^-})$	$\rm H^- + h\nu \rightarrow H + e^-$	McLaughlin et al. (2017)
	$\sigma_{\rm bf}({\rm H})$	$\rm H + h\nu \rightarrow H^+ + e^-$	Method as in Kurucz (1970) based on Karzas & Latter (1961 and Gingerich (1964))
	$\sigma_{\rm bf}({\rm H_2^+})$	$\rm H_2^+ + h\nu \rightarrow H^+ + H$	Lebedev et al. (2003)
	$\sigma_{\rm bf}({\rm He})$	$\rm He + h\nu \rightarrow He^+ + e^-$	Method as in Kurucz (1970) based on Gingerich (1964) and Hunger & van Blerkom (1967)
	$\sigma_{\rm bf}({\rm He^+})$	$\rm He^+ + h\nu \rightarrow He^{++} + e^-$	Hunger & van Blerkom (1967)
Bound–bound	$\sigma_{\rm bb}({\rm H})$	$\rm H + h\nu \rightarrow H^*$	Kurucz (1970) including Stark broadening
CIA	$\sigma_{\rm CIA}({\rm H_2/H_2})$	$\rm H_2 + H_2 + h\nu \rightarrow H_2 + H_2$	$200\,{\rm K} < T < 3000\,{\rm K}$, $20\,{\rm cm^{-1}} < \tilde\nu < 10,000\,{\rm cm^{-1}}$ Abel et al. (2011)
	$\sigma_{\rm CIA}({\rm H_2/H})$	$\rm H_2 + H + h\nu \rightarrow H_2 + H$	$1000\,{\rm K} < T < 2500\,{\rm K}$, $100\,{\rm cm^{-1}} < \tilde\nu < 10,000\,{\rm cm^{-1}}$ Gustafsson & Frommhold (2003)
	$\sigma_{\rm CIA}({\rm H_2/He})$	$\rm H_2 + He + h\nu \rightarrow H_2 + He$	$200\,{\rm K} < T < 9900\,{\rm K}$, $20\,{\rm cm^{-1}} < \tilde\nu < 20,000\,{\rm cm^{-1}}$ Abel et al. (2012)
	$\sigma_{\rm CIA}({\rm H/He})$	$\rm H + He + h\nu \rightarrow H + He$	$1500\,{\rm K} < T < 10,000\,{\rm K}$, $50\,{\rm cm^{-1}} < \tilde\nu < 11,000\,{\rm cm^{-1}}$ Gustafsson & Frommhold (2001)
Bound–free free–free	C, N, O Ne, Na, Mg Al, Si, S Ar, Ca, Cr Mn, Fe, Ni	$\rm X + h\nu \rightarrow X^+ + e^-\ X + e^- + h\nu \rightarrow X + e^-$	Opacity project: Seaton (1995) for $\log(T) \geqslant 3.6$
Bound–free	CI, NI OI, MgI AlI, SiI	$\rm X + h\nu \rightarrow X^+ + e^-$	Method as in Kurucz (1970) based on Peach (1970) and Henry (1970) for $\log(T) < 3.6$

Note. Here X denotes the generic atom/ion. Molecular absorption sources are described in Table 2.

for the free–free (Bell & Berrington 1987) and bound–free (Wishart 1979 for $\lambda < 1.6419\,\mu{\rm m}$) cross sections are a classic reference study of $\rm H^-$ that is used in most opacity codes.

In this work, we use the recent study carried out by McLaughlin et al. (2017) to revise the photodetachment cross section of $\rm H^-$. McLaughlin et al. (2017) combined R-matrix calculations and comparison to available experimental data to build an $\rm H^-$ photodetachment cross section that is accurate over a wide range of photon energies and takes into account a series of autodetaching shape and Feshbach resonances at

photon energies ranging from 10.92 to 14.35 eV. As discussed by McLaughlin et al. (2017) and shown in Figure 1, the simple fit to the Wishart (1979) calculations cannot reproduce the behavior of the cross section in the region of the autodetaching resonances beyond 10 eV.

3.2. Collision-induced Absorption

The CIA is caused by collisions of molecules and atoms in a gas of relatively high density (Frommhold 1994).

Table 2
Spectral Line Data for Molecular Absorption

Molecule	References	Molecule	References
HF	Coxon & Hajigeorgiou (2015); Li et al. (2013)	CaO	Yurchenko et al. (2016)
HCl	Li et al. (2011)	CH_3	Adam et al. (2019)
CH	Masseron et al. (2014)	CH_3Cl	Owens et al. (2018)
C_2	McKemmish et al. (2020); Yurchenko et al. (2018c)	CP	Qin et al. (2021); Ram et al. (2014)
CN	Syme & McKemmish (2021)	H_2	Roueff et al. (2019)
CO	Somogyi et al. (2021); Li et al. (2015)	H_2S	Azzam et al. (2016)
OH	Yousefi et al. (2018); Brooke et al. (2016)	KCl	Barton et al. (2014)
SiO	Yurchenko et al. (2022)	KF	Frohman et al. (2016)
TiO	McKemmish et al. (2019)	KOH	Owens et al. (2021)
VO	McKemmish et al. (2016)	LiCl	Bittner & Bernath (2018)
CrH	Diatomic database of P.F. Bernath (http://bernath.uwaterloo.ca)	MgF	Hou & Bernath (2017)
FeH	Dulick et al. (2003)	MgO	Li et al. (2019)
YO	Smirnov et al. (2019)	N_2	HITRAN; Gordon et al. (2022)
ZrO	Van Eck et al. (2017); Plez (2012)	NaCl	Barton et al. (2014)
H_2O	Polyansky et al. (2018)	NaF	Frohman et al. (2016)
HCN	Harris et al. (2006)	NaO	Mitev et al. (2022)
C_3	Jorgensen et al. (1989)	NaOH	Owens et al. (2021)
CO_2	Yurchenko et al. (2020a)	NH_3	Coles et al. (2019); Al Derzi et al. (2015)
SO_2	Underwood et al. (2016)	NO	Qu et al. (2021)
C_2H_2	Chubb et al. (2020)	NS	Yurchenko et al. (2018b)
AlH	Yurchenko et al. (2018d)	PH	Langleben et al. (2019)
AlO	Bowesman et al. (2021); Patrascu et al. (2015)	PH_3	Sousa-Silva et al. (2014)
CaH	Owens et al. (2022)	PN	Yorke et al. (2014)
CH_4	Yurchenko et al. (2017a); Yurchenko & Tennyson (2014)	PO	Prajapat et al. (2017)
CS	Paulose et al. (2015)	PS	Prajapat et al. (2017)
LiH	Coppola et al. (2011)	ScH	Chubb et al. (2021); Lodi et al. (2015)
MgH	Owens et al. (2022)	SiH_4	Owens et al. (2017)
TiH	Burrows et al. (2005)	SiO_2	Owens et al. (2020)
NaH	Rivlin et al. (2015)	SiS	Upadhyay et al. (2018)
NH	Fernando et al. (2018); Brooke et al. (2015)	LiF	Bittner & Bernath (2018)
SH	Gorman et al. (2019)	O_2	Chubb et al. (2021); Gordon et al. (2017)
SiH	Yurchenko et al. (2017b)	OCS	Gordon et al. (2022)
AlCl	Bernath (2020)	H_3^+	Mizus et al. (2017)
AlF	Bernath (2020)	H_3O^+	Yurchenko et al. (2020b)
BeH	Darby-Lewis et al. (2018)	HeH^+	Amaral et al. (2019)
C_2H_4	Mant et al. (2018)	LiH^+	Coppola et al. (2011)
CaF	Hou & Bernath (2018)	OH^+	Hodges & Bernath (2017)
CS_2	HITRAN; Gordon et al. (2022)	SO	HITRAN; Gordon et al. (2022)
HI	HITRAN; Gordon et al. (2022)	ClO	HITRAN; Gordon et al. (2022)
HBr	HITRAN; Gordon et al. (2022)	O_3	HITRAN; Gordon et al. (2022)

Note. Most of the monochromatic absorption cross sections (except for C_3 and ZrO) are calculated using the EXOCROSS tool, available in the ExoMol (https://www.ExoMol.com/data/molecules/) database, from the corresponding line lists. Line broadening accounts for thermal Doppler and microturbulent velocity.

Because hydrogen and helium gases dominate the atmospheres of giant stars and brown dwarfs, collision complexes such as H_2/H_2, H_2/H, H_2/He, and H/He may contribute significantly to absorption in these layers. In this work, we adopt the latest parameterization setup in the HITRAN spectroscopic database (Karman et al. 2019). In particular, we adopt the results from Abel et al. (2011) for H_2/H_2, Gustafsson & Frommhold (2003) for H_2/H, Abel et al. (2012) for H_2/He, and Gustafsson & Frommhold (2001) for H/He.

As discussed by Abel et al. (2011) and shown in Figure 2 (left panel), the H_2 rotational fundamental band and first-overtone structures at the lowest temperature ($T = 1000$ K) are particularly pronounced, but as the temperature rises, the interband minima shrink, and the H_2 bands blend more and more. There are substantial differences between the results of Abel et al. (2011) and the earlier calculations of Borysow et al. (1997), especially for higher temperatures ($T > 1000$ K). The inconsistencies are most likely due to a less accurate

characterization of the induced dipole surface in older CIA studies, the results of which are adopted in opacity calculations by Marigo & Aringer (2009) and Ferguson et al. (2005). Similar considerations apply to H_2/He CIA (Figure 2, right panel).

3.3. Molecular Absorption

This work represents a substantial advancement over Marigo & Aringer (2009) in terms of molecular absorption (see Table 2). We extend the number of absorbing molecules to 80 (in Marigo & Aringer 2009, ÆSOPUS 1.0, there were 20), and we carry out a systematic update of the monochromatic cross sections, $\sigma_j(\nu)$. The update is primarily based on the ExoMol line list database (Tennyson & Yurchenko 2012) and its public tools, in particular the software EXOCROSS to compute the absorption cross sections (Yurchenko et al. 2018a). Data from HITRAN are also included (Gordon et al. 2022).

Photodetachment of H⁻
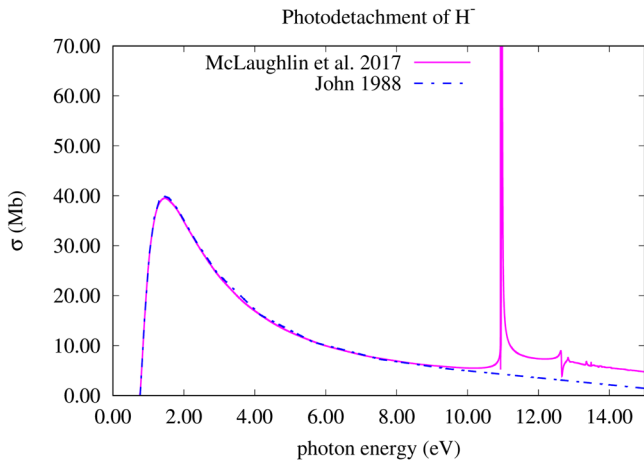
Figure 1. Photodetachment cross section from McLaughlin et al. (2017; solid line) compared to John's (1988) fit of the cross-section data from Wishart (1979; dashed line). As can be seen, the latter does not account for autodetaching resonances at photon energies above 10 eV. The cross section σ is in units of 10^6 barn (Mb).

Table 2 contains the complete record of absorbing molecules, together with the corresponding line list sources. For each molecular species included in our code, the monochromatic cross section, $\sigma_j(\nu)$, is taken from OS files produced for a selected frequency grid that are calculated directly from the corresponding line list.

As an example, Figure 3 depicts the cross sections of two relevant molecules in the atmospheres of red giants, which are characterized by a photospheric carbon-to-oxygen ratio[5] C/O < 1. We compare H_2O and TiO absorption from different line lists used in ÆSOPUS 1.0 (Marigo & Aringer 2009) and the current version, ÆSOPUS 2.0.

The POKAZATEL line list for water (Polyansky et al. 2018) has nearly 6×10^9 lines, while BT2 (Barber et al. 2006) includes $\approx 500 \times 10^6$ transitions. The POKAZATEL line list, in particular, produces much weaker absorption in the near-UV region than BT2, which is supported by the findings of a recent study of ultraviolet terrestrial atmospheric absorption (Lampel et al. 2017). Furthermore, unlike BT2, the POKAZATEL cross sections become progressively flattened with increasing temperature as a result of a more comprehensive treatment, including high J states and vibrational hot bands (see Polyansky et al. 2018 for a thorough discussion). Overall, these differences in monochromatic cross sections may have a significant impact on the resulting Rosseland mean opacities.

Below, we will briefly review two specific aspects of our procedure for treating molecular absorption.

Optimized OS—When computing Rosseland mean opacities, the frequency grid must be carefully chosen to ensure both fast performance and accuracy. As thoroughly discussed in Marigo & Aringer (2009), we use the Helling & Jørgensen (1998) algorithm to optimize the frequency distribution in the OS technique.

As demonstrated by our earlier tests in Marigo & Aringer (2009), computing time increases almost linearly with OS frequency grid size, n_{OSgrid}, while gain in precision does not, resulting in Rosseland mean opacities that vary only marginally beyond a certain threshold of a few thousand frequency points.

The results presented here are obtained with an OS frequency grid containing $n_{\mathrm{OSgrid}} = 5365$ points,[6] yielding a favorable accuracy/computing-time ratio.

In this work, we optimize the frequency grid selection even further by focusing on the lower and upper limits of the integral in Equation (4), which formally defines the Rosseland mean opacity. In Marigo & Aringer (2009), we used constant integration limits corresponding to wavenumbers $\tilde{\nu}_{\min} = 10$ and $\tilde{\nu}_{\max} = 2 \times 10^5 \, \mathrm{cm}^{-1}$. These values adequately cover the frequency range that is relevant for the temperatures under consideration. We can, however, improve the selection of the integration extremes. Following Seaton et al. (1994), we note that κ_{R} can be easily calculated with

$$\frac{1}{\kappa_{\mathrm{R}}(\rho, T)} = \int_{u_{\min}}^{u_{\max}} \frac{F_{\mathrm{R}}(u)}{\kappa(u)} du, \qquad (5)$$

where the weighting function is expressed as

$$F_{\mathrm{R}}(u) = \frac{15}{4\pi^4} u^4 \exp(-u) / [1 - \exp(-u)]^2. \qquad (6)$$

Here ν is the photon frequency, and $u = h\nu/(k_{\mathrm{B}}T)$ is the normalized photon energy. The integration extremes, $u_{\min}$ and $u_{\max}$, should be chosen in such a way that they vastly encompass the domain where the function $F_{\mathrm{R}}(u)$ is not zero.

As shown in Figure 4 (left panel), setting $u_{\min} = 0.1$ and $u_{\max} = 20$ satisfies this requirement, as these correspond to $\simeq 0.001$ and $\simeq 99.998$ percentiles of $F_{\mathrm{R}}(u)$, respectively. Because the normalized energy u varies with temperature, we can make the integration extremes dynamic (see Figure 4, right panel), rather than keeping them fixed for any value of T. In this way, we can eliminate unnecessary frequency points that are outside the range $[u_{\min}, u_{\max}]$, which has the added benefit of shortening the numerical integration. This will be especially important for speeding up on-the-fly opacity computations through our public web interface.

Finally, it is worthwhile to investigate the impact of further reducing the number of frequency points below the reference grid with a nominal size of $n_{\mathrm{OSgrid}} = 5365$. For this purpose, we tested two additional frequency distributions with $n_{\mathrm{OSgrid}} = 2358$ and 1458, both built using Helling & Jørgensen's (1998) optimization scheme. Figure 5 illustrates the results. It is clear that reducing the frequency grid by a factor of about 2.3 or 3.7 has a limited impact, resulting in a precision loss that is mostly confined to the range of 0.01–0.02 dex in $\log(\kappa_{\mathrm{R}})$. At the same time, the increase in computational speed is noticeable. When using frequency grids with $n_{\mathrm{OSgrid}} = 5365$, 2358, and 1458 points, the CPU time required to compute the same opacity table on a laptop is 157, 69, and 48 s, respectively. We conclude that a faster performance is possible with a minimal precision loss in κ_{R}. The next step is to assess the impact of these opacity differences on stellar models. Section 5 addresses this critical aspect.

Line broadening—We account for line broadening due to the thermal Doppler effect and nonthermal contribution of

---

[5] C/O is the ratio of C to O abundances (in number) at the star's photosphere.

[6] Helling & Jørgensen (1998) investigated the reliability of the radiative transfer solution in hydrostatic MARCS models of cool giant star atmospheres as a function of frequency grid size. Moving from $n_{\mathrm{OSgrid}} = 22,432$ to 5608 points, the maximum deviation in surface temperature does not exceed 8 K (see their Table 1 and Figure 3).
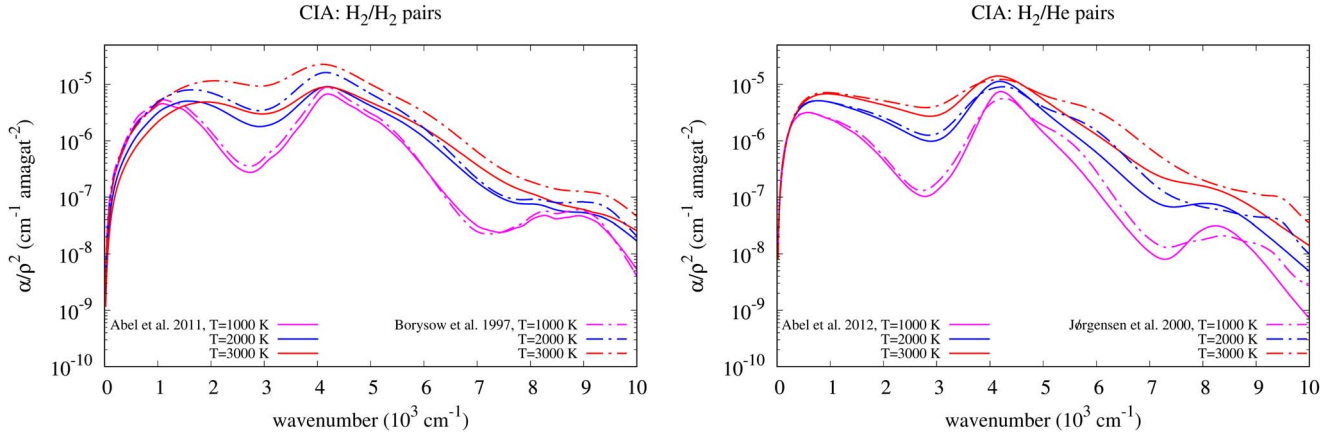
Figure 2. The CIA of H_2/H_2 and H_2/He pairs. Following standard notation, the absorption coefficient α is normalized by gas density squared. The data adopted in the current version, ÆSOPUS 2.0 (solid line; Abel et al. 2011 for H_2/H_2 and Abel et al. 2012 for H_2/He), are compared to those used in ÆSOPUS 1.0 (dashed–dotted line; Borysow et al. 1997 for H_2/H_2 and Jørgensen et al. 2000 for H_2/He) for three temperature values.
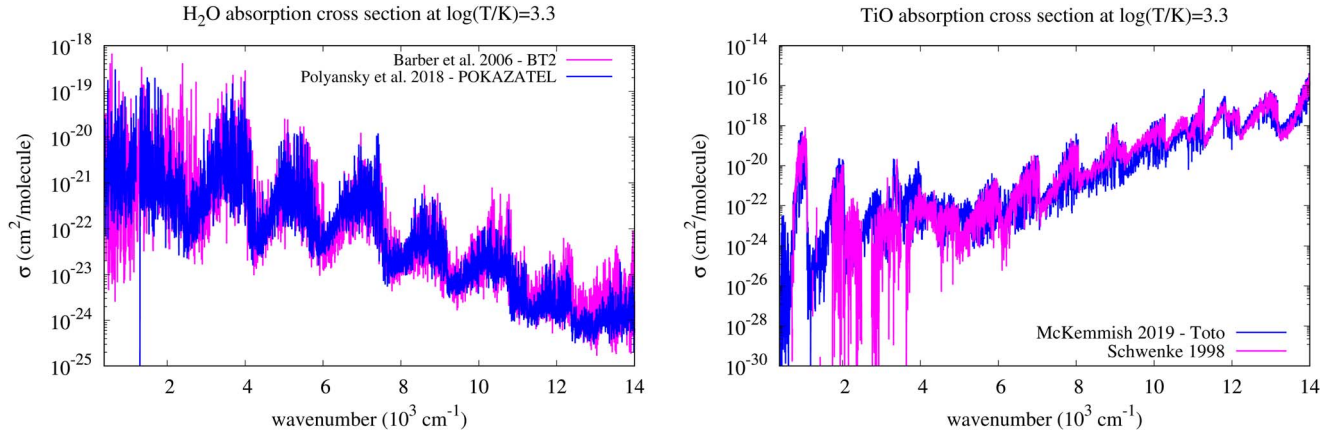
Figure 3. Absorption cross section of two important molecules in the cool atmospheres of O-rich giants and supergiants, namely, H_2O (left panel) and TiO (right panel). We compare the ExoMol recommended line lists (blue) adopted in this work with earlier data (magenta) used in ÆSOPUS 1.0. Line broadening due to the thermal Doppler effect and microturbulent velocity was used for both molecules' transitions.
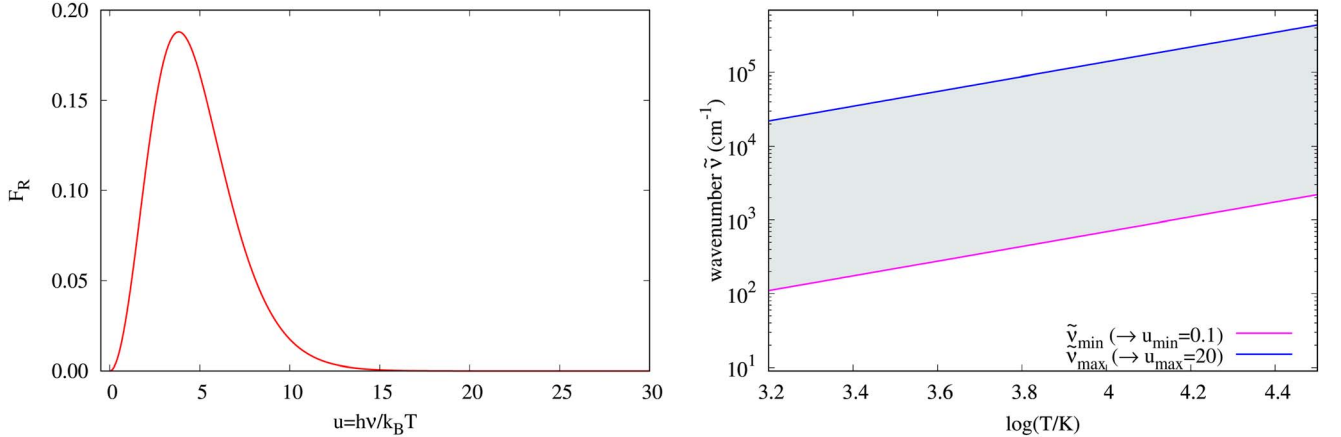

Figure 4. Left: weighting function, $F_R(u)$, in the integral of Equation (5). Right: dynamic integration limits in wavenumber $\tilde{\nu}$, dependent on temperature, used for the integration of the Rosseland mean opacity. Normalized energies $u_{min} = 0.1$ and $u_{max} = 20$ correspond to $\tilde{\nu}_{min}$ and $\tilde{\nu}_{max}$.

microturbulent velocities by constructing a normalized broadening profile, $\phi(\nu)$, according to the equation

$$\phi(\nu) = \frac{1}{\Delta_\nu \sqrt{\pi}} e^{-\left(\frac{\nu - \nu_0}{\Delta_\nu}\right)^2}, \tag{7}$$

where ν_0 is the line center position in frequency, and Δ_ν is the line width, computed with

$$\Delta_\nu = \frac{\nu_0}{c} \sqrt{\frac{2k_B T}{m} + \xi^2}. \tag{8}$$
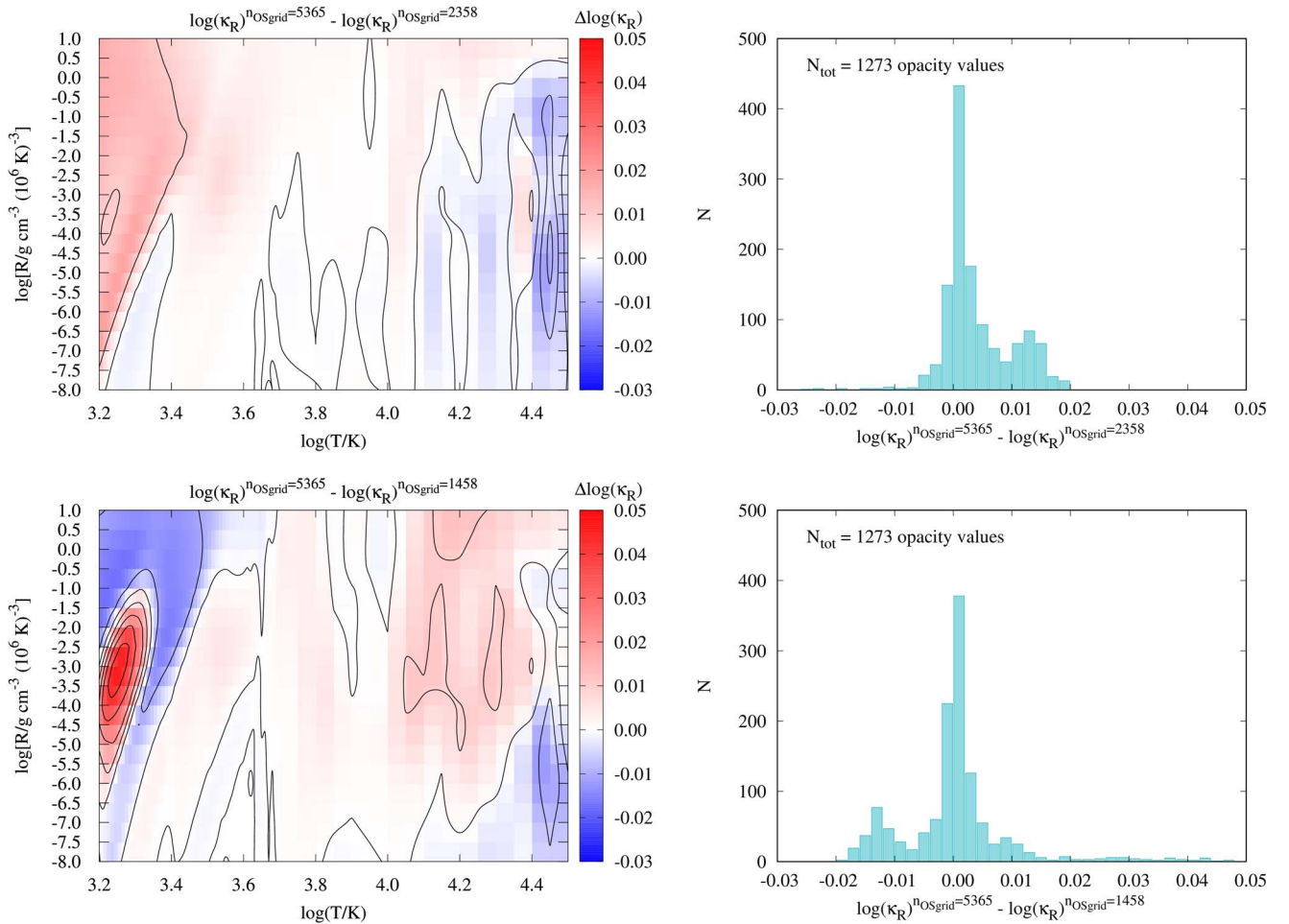
Figure 5. Differences in Rosseland mean opacities between the reference frequency grid with $n_{OSgrid} = 5365$ points and two test cases with $n_{OSgrid} = 2358$ and 1458 (top and bottom panels, respectively). The chemical composition assumes $X = 0.7$, $Z = 0.0165$, with scaled-solar elemental abundances according to (MBS22). Left panels: maps of opacity differences across the whole R–T extension of a typical table. Contour levels are distributed every 0.01 dex in $\Delta \log(\kappa_R)$. Right panels: distribution of opacity differences with respect to the reference frequency grid calculated over the entire sample of $N_{tot} = 1273$ opacity values in the table.

Here c is the speed of light, k_B is the Boltzmann constant, m is the molecule's mass, and ξ is the microturbulent velocity, which is set to $2.5 \, \mathrm{km \, s^{-1}}$. This value is compatible with the microturbulent velocities inferred from stellar spectra of giant and dwarf stars (e.g., Plez et al. 1993; Vanture & Wallerstein 2002; Mucciarelli 2011).

We emphasize that the EXOCROSS program employs a Gaussian profile, rather than a Voigt profile. This should not have a noticeable effect on the Rosseland mean opacity, given that the many different opacity sources overlap in ways that minimize any effects of ignoring the far wings of molecular lines. In the case of planetary and brown dwarf atmospheres with little or no ionization and H appearing primarily as H_2, neglecting the line-extended wings may instead be more significant.

4. Discussion of the Results

Below, we will analyze the new results, comparing them with those obtained with the initial version of ÆSOPUS and other opacity data in the literature.

4.1. Scaled-solar Mixtures

In stellar models, scaled-solar mixtures represent a reference choice for several applications. The chemical composition of the

Sun (derived from the Sun's spectrum and/or chemical analyses of primitive meteorites) has undergone numerous revisions over the years. Table 3 lists the major solar mixtures in chronological order, beginning with the oldest (Anders & Grevesse 1989) and progressing to the most recent one (MBS22). As can be seen, the estimated current metallicity of the Sun, $Z_{\odot}$, shows a decreasing trend over time, passing from a maximum of $Z_{\odot} = 0.0194$ (AG89) to a minimum of around $Z_{\odot} \simeq 0.012$–0.014 (Grevesse et al. 2007; Asplund et al. 2009, 2021). Such a decrease of $Z_{\odot}$ has entailed severe difficulties in reproducing the helioseismological constraints and the global parameters of the Sun at the present time (e.g., Serenelli et al. 2009). MBS22 most recent revision of the standard composition of the Sun indicates a new increase in the present-day metallicity (primarily due to greater abundances of oxygen and carbon) up to $Z_{\odot} = 0.0165$, with a significant improvement in the standard solar model's ability to reproduce observational data. The calibration of the solar model with our PARSEC code (Bressan et al. 2012) based on the new ÆSOPUS 2.0 opacities is currently in progress.

Figure 6 displays κ_R as a function of temperature for scaled-solar mixtures according to all solar compositions in Table 3. We note that the present-day solar photospheric carbon-to-oxygen ratio, C/O, varies between sources, from a minimum of $C/O \simeq 0.427$ in AG89 to larger values such as $C/O \simeq 0.718$
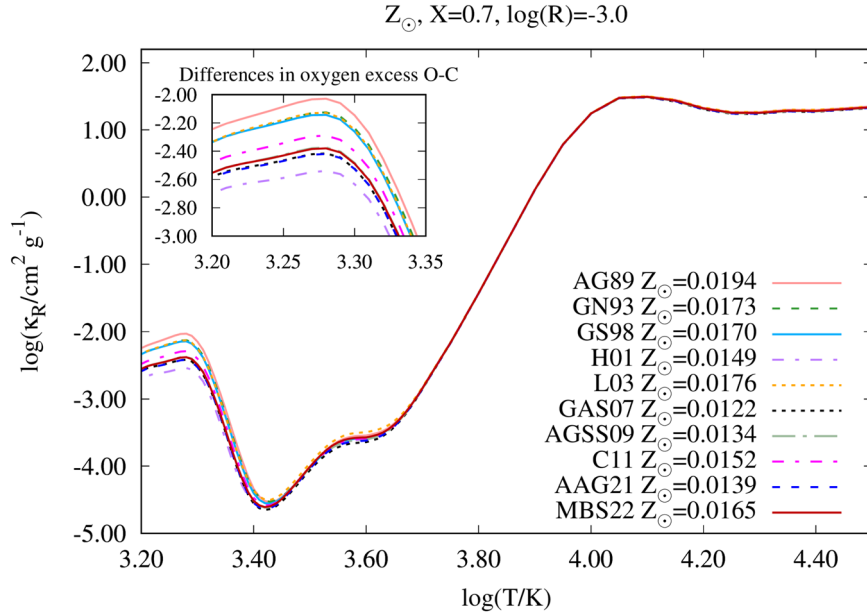
Figure 6. ÆSOPUS 2.0 Rosseland mean opacity as a function of temperature, with $\log(R) = -3$. The adopted chemical composition is defined by $X = 0.7$ and $Z = Z_\odot$ according to various compilations of the solar mixture (see Table 3). As highlighted in the inset, the largest differences occur at $\log(T/K) \lesssim 3.4$, where water absorption dominates the opacity.

Table 3
Main Solar Chemical Compositions in Literature

References	$(Z/X)_\odot$	$Z_\odot$	$(C/O)_\odot$	$(O - C)_\odot$[a]	$(C/O)_{crit}$[b]
Anders & Grevesse (1989) (AG89)	0.02742	0.0194	0.427	8.688	0.958
Grevesse & Noels (1993) (GN93)	0.02444	0.0173	0.479	8.587	0.952
Grevesse & Sauval (1998) (GS98)	0.02308	0.0170	0.490	8.538	0.947
Holweger (2001) (H01)[c]	0.02094	0.0149	0.718	8.187	0.937
Lodders (2003) (L03)	0.01760	0.0132	0.501	8.388	0.929
Grevesse et al. (2007) (GAS07)	0.01653	0.0122	0.537	8.326	0.929
Asplund et al. (2009) (AGSS09)	0.01813	0.0134	0.549	8.344	0.934
Caffau et al. (2011) (C11)[d]	0.02070	0.0152	0.575	8.414	0.938
Asplund et al. (2021) (AAG21)	0.01867	0.0139	0.589	8.304	0.888
Magg et al. (2022) (MBS22)[e]	0.02250	0.0165	0.617	8.354	0.934

Notes. For each mixture, the solar metallicity–to–hydrogen abundance ratio $(Z/X)_\odot$, the present-day total metallicity $Z_\odot$ (in mass fraction), the ratio $(C/O)_\odot$, the oxygen excess $(O - C)_\odot$, and $(C/O)_{crit}$ are indicated for comparison. Carbon and oxygen abundances are expressed as number fractions.
[a] Following a standard notation, we define $(O - C)_\odot = \log(n_C/n_H - n_O/n_H) + 12$, where n_C, n_O, and n_H denote the number densities of carbon, oxygen, and hydrogen in the Sun's photosphere, respectively.
[b] This abundance ratio is defined as $(C/O)_{crit} = 1 - n_{Si}/n_O$ (Ferrarotti & Gail 2006). It marks a critical boundary for the gas molecular chemistry and opacity in the range $3.2 \leqslant \log(T) \leqslant 3.6$. For $C/O_{crit} \lesssim C/O \lesssim 1$, the opacity enters a narrow and deep minimum (see Marigo & Aringer 2009).
[c] Revision of C, N, O, Ne, Mg, Si, and Fe. All other elemental abundances are taken from (GS98).
[d] Revision of Li, C, N, O, P, S, K, Fe, Eu, Hf, Os, and Th. All other elemental abundances are taken from (GS98).
[e] Revision of all nuclides from C to Ni; Ba abundance is from Gallagher et al. (2020); Eu, Hf, Os, and Th come from C11; and all other elemental abundances are taken from (GS98).

of H01 and, more recently, $C/O \simeq 0.617$ in MBS22. These variations may produce a significant impact on molecular chemistry and opacity mostly for $\log(T/K) \lesssim 3.4$. More specifically, at these temperatures, κ_R is dominated by the opacity bump caused by the H_2O molecule, the magnitude of which is extremely sensitive to the excess of oxygen atoms over those of carbon, $O - C$. This parameter, which is also listed in Table 3, represents the amount of oxygen that is not locked in the extremely stable CO molecule and is available for the formation of important O-bearing absorbing species, such as H_2O, AlO, VO, TiO, and ZrO. As a result, the larger the $(O - C)_\odot$, the higher the κ_R because more oxygen is free to be trapped in H_2O.

This is evident when we compare the opacity curves of MBS22 and GS98 in Figure 6. Despite having a similar solar metallicity $(Z_\odot \simeq 0.0165$–$0.0170)$, the opacity peak due to water at $T \simeq 2000$ K in GS98 is higher due to a greater oxygen excess, $(O - C)_\odot \simeq 8.538$, compared to $(O - C)_\odot \simeq 8.354$ in MBS22. At the same time, despite significant differences in $Z_\odot$, AGSS09 and MBS22 exhibit an almost identical opacity profile at 1600 K $\lesssim T \lesssim 2500$ K owing to a comparable $(O - C)_\odot \simeq 8.34$–$8.35$.

4.2. Comparison of ÆSOPUS 1.0 and 2.0 and Ferguson et al. (2005)

Figure 7 will help us appreciate the differences brought about by our update to the opacity sources. For this purpose, in the left panels, we compare three sets of opacity calculations:
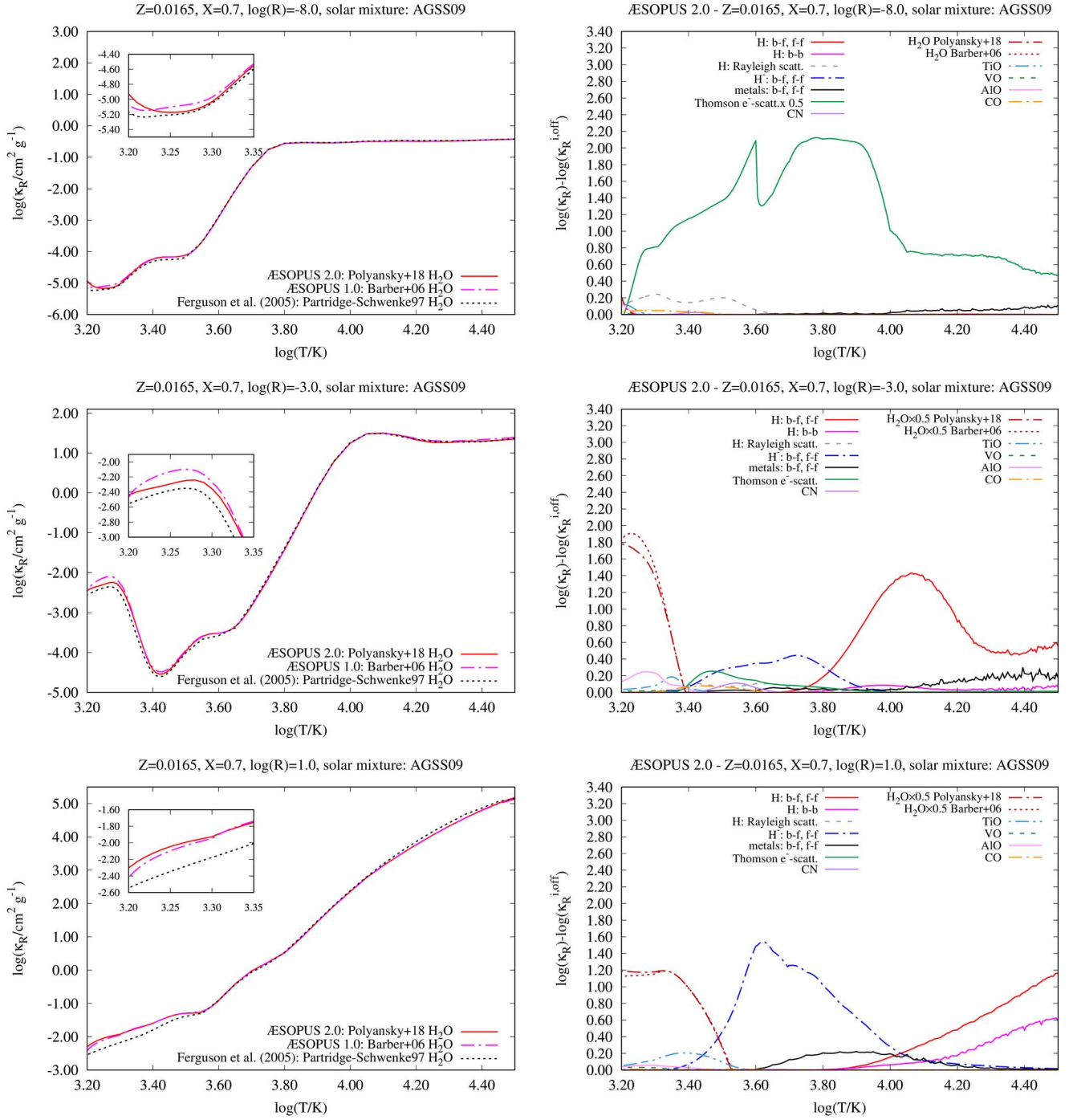
Figure 7. Rosseland mean opacity and major opacity sources as a function of temperature T and for three values of R. The adopted composition is assumed to have $Z = 0.0165$, $X = 0.7$, and the metal abundances scaled to solar following AGSS09. In the left panels, as indicated in the legends, the three curves correspond to different opacity calculations. The insets zoom in on the most pronounced opacity variations for temperatures below about 2240 K. Except for the lowest-density case (top panels with $\log(R) = -8$), where Thomson e^- scattering dominates the opacity, the differences are primarily due to different water absorption line lists and the line broadening scheme used. Right panels: contributions to the total Rosseland mean opacity from various opacity sources, as derived from AESOPUS 2.0 calculations shown in the left panel. Each curve corresponds to $\log(\kappa_R) - \log(\kappa_R^{i,\mathrm{off}})$, where κ_R is the full opacity including all opacity sources considered here, and $\kappa_R^{i,\mathrm{off}}$ is the reduced opacity obtained by excluding the specific absorbing species. See the text for more details.

the current implementation (ÆSOPUS 2.0), the first version (Marigo & Aringer 2009; ÆSOPUS 1.0), and Ferguson et al. (2005, hereafter F05). The reference solar mixture is from AGSS09.

It is also useful to refer to the right panels, which display temperature windows where the main opacity sources make a significant contribution. For each opacity source i, we compute the quantity $\log(\kappa_R) - \log(\kappa_R^{i,\mathrm{off}})$, where κ_R is the total

Rosseland mean opacity including all opacity sources considered here, and $\kappa_R^{i,\mathrm{off}}$ is the reduced opacity obtained by ignoring the species i. This specific notation allows us to highlight the temperature domains where different opacity sources contribute the most.

The case with $\log(R) = -8$ (top panels) corresponds to a very low density regime in which the opacity is almost entirely dominated by Thomson electron scattering, with some
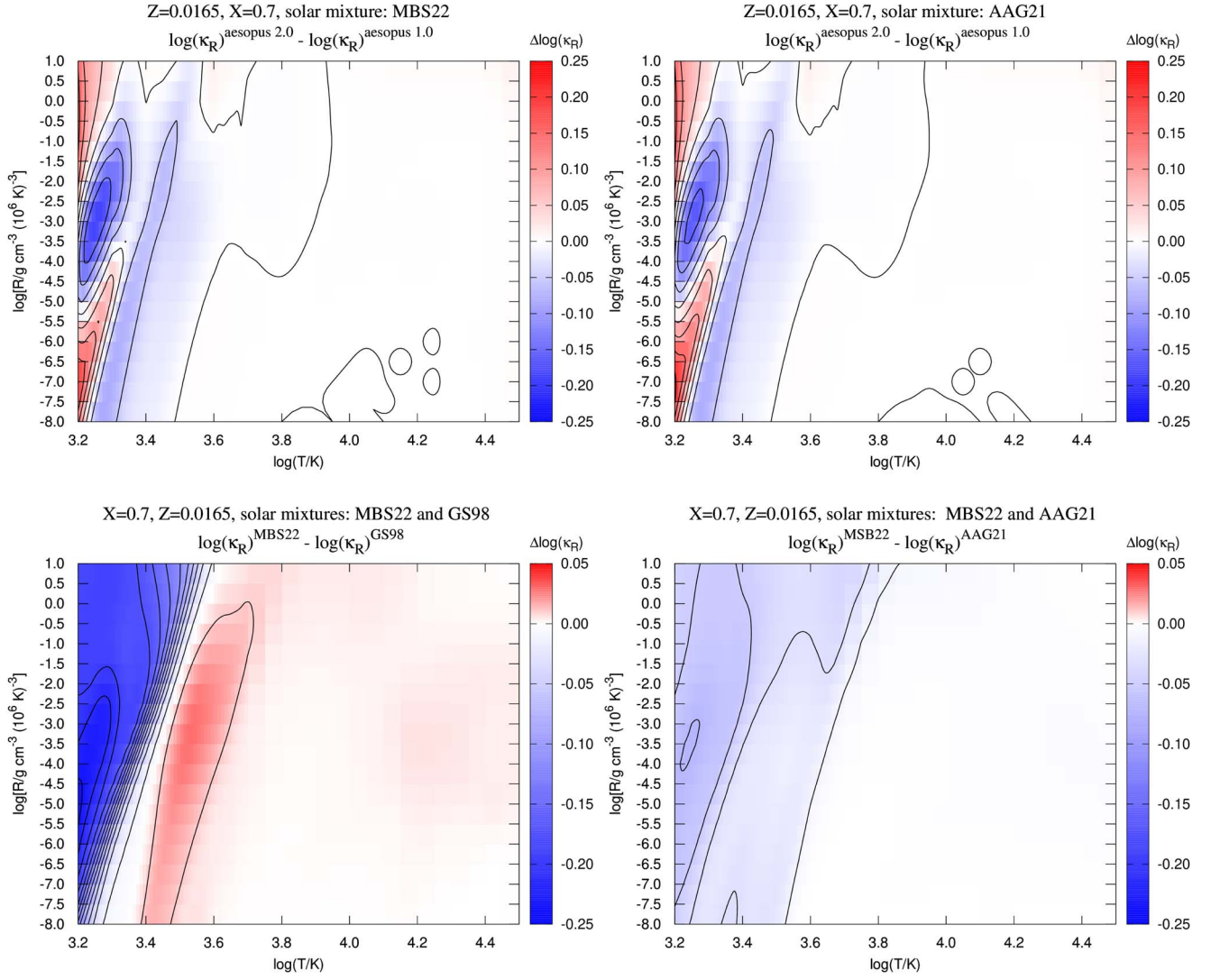
Figure 8. Comparison of Rosseland mean opacities across the entire extension of a typical table, assuming $X = 0.7$ and $Z = 0.0165$. Top panels: differences between ÆSOPUS 2.0 and ÆSOPUS 1.0, mainly due to the updates and expansion of molecular absorption. Solar compositions from MBS22; left) and (AAG21; right) are assumed. Contour levels map a 0.05 dex difference in $\log(\kappa_R)$. Bottom panels: differences caused by the choice of solar mixture. Comparison is made between GS98 and MBS22 (left) or AAG21 and MBS22 (right). Version ÆSOPUS 2.0 is adopted. The grid of contour levels is distributed every 0.02 dex difference in $\log(\kappa_R)$.

contribution from H Rayleigh scattering for $\log(T) < 3.6$. Molecular absorption plays a minor role. This explains the very small differences between the various sets of opacity calculations. In the case with $\log(R) = -3$ (middle panels), differences start to appear for $\log(T/\mathrm{K}) \lesssim 3.6$. They remain moderate in the range $3.4 \lesssim \log(T/\mathrm{K}) \lesssim 3.6$, which is likely due to the revision of the opacity of the CN molecule. In terms of CN, this work employs the line list of Syme & McKemmish (2021), Marigo & Aringer (2009) used the data from Jørgensen (1997), and Ferguson et al. (2005) adopted the line list of Jørgensen & Larsson (1990).

We find that the revision of the H⁻ photodetachment cross section (McLaughlin et al. 2017) produces very small differences in the resulting κ_R when compared to previous predictions (Wishart 1979) at both intermediate ($\log(R) = -3$; middle panels) and high ($\log(R) = 1$; bottom panels) densities. This fact can be explained as follows. The resonances of H⁻ photodetachment are located at $h\nu > 10$ eV, which corresponds to normalized photon energies $u > u_{\mathrm{res}}$, with the exact value of u_{res} depending on the gas temperature. It is easy to see that at the temperatures ($3000 \lesssim T/\mathrm{K} \lesssim 8000$), where H⁻ contributes

substantially to κ_R, u_{res} varies in the range $38.7 \gtrsim u_{\mathrm{res}} \gtrsim 14.5$, where the weighting function F_R of the Rosseland mean opacity is very small or close to zero (see Figure 4 and Equation (5)). As a result, the resonances have only a minor effect on the integral that defines κ_R.

At lower temperatures, in the interval $3.2 \lesssim \log(T/\mathrm{K}) \lesssim 3.35$, and examining the case with $\log(R) = -3$ (middle panels), Figure 7 clearly shows that the ÆSOPUS 2.0 revised opacity lies somewhere in between ÆSOPUS 1.0 and F05. In the latter temperature range, κ_R is dominated by water molecular absorption; therefore, it is affected by the adopted H_2O line list. We recall that F05 adopted Partridge & Schwenke (1997) and Marigo & Aringer (2009) used the BT2 transitions from Barber et al. (2006), whereas in this work, we employ the POKAZATEL line list from Polyansky et al. (2018; see Figure 3). Different line broadening schemes are likely to cause additional discrepancies. Authors F05 used a thermal Doppler profile; we do the same but also include the effect of microturbulence velocity (see Equation (8)).

It is worthwhile to compare the differences in Rosseland mean opacity caused by changes in the input data (e.g.,
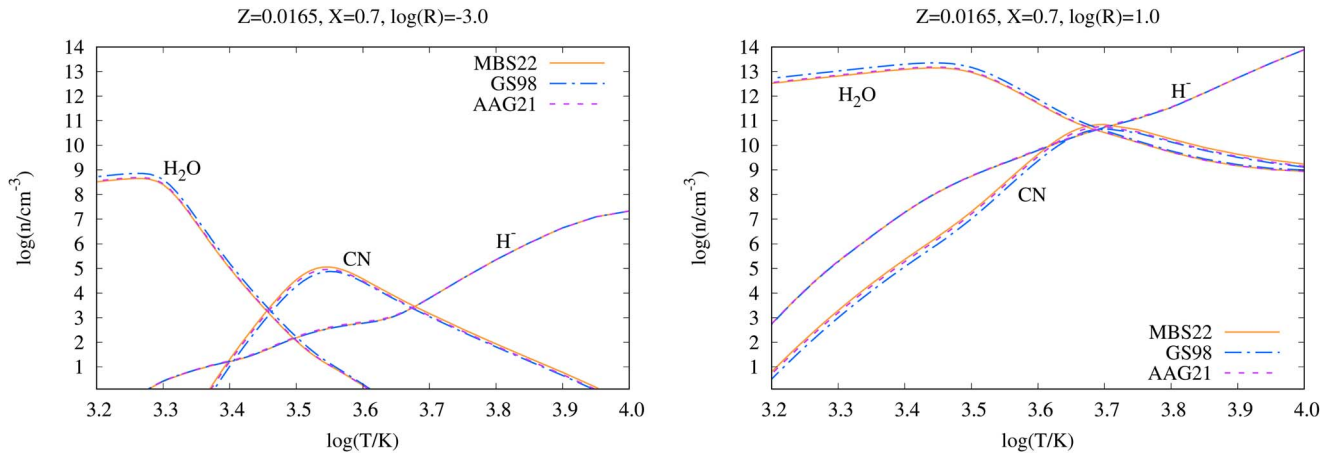
Figure 9. Number densities of H_2O, CN, and H^- as a function of temperature for two R parameter values. ÆSOPUS 2.0 predictions are shown for three solar mixtures, namely, GS98, AAG21, and MBS22.

molecular line lists, line profiles, and other opacity sources). Figure 8 illustrates a few examples. Looking at the top panels, we can see that the opacity changes from ÆSOPUS 1.0 to ÆSOPUS 2.0 are distinguishable but not dramatic. The water opacity bump, in particular, is reduced by up to 0.25 dex. As expected, these changes are largely independent of the solar composition; using MBS22 (top left panel) or AAG21 (top right panel) produces nearly identical maps of opacity difference.

4.3. Changes in Solar Mixture Effects

Finally, we investigate the main opacity differences caused by different solar mixture options while keeping the input opacity data constant. The bottom panels of Figure 8 show the results of a few tests. Three alternatives are being considered: GS98, AAG21, and MBS22, all with the same metallicity $Z = 0.0165$ and hydrogen abundance $X = 0.7$. The largest differences appear at $\log(T/K) < 3.8$, where molecular absorption becomes significant and is influenced by the relative distribution of elemental abundances. To aid the discussion, Figure 9 depicts the number densities of three species (H_2O, CN, and H^-) that have been shown to significantly contribute to the Rosseland mean opacity at these temperatures.

Let us first focus on the role of H^-, the abundance of which is critically dependent on the availability of free electrons provided by low ionization potential atoms, particularly Mg, Si, and Fe (see Figure 22 of Marigo & Aringer 2009). The concentration of H^- in the three solar mixtures is nearly identical, with minor differences. The reason for this is that the total abundance of the major electron donors (Mg, Si, and Fe) varies little in the three cases, resulting in essentially the same opacity contribution from H^- for both $\log(R) = -3.0$ and 1.0.

Another source of opacity is the absorption of CN, the concentration of which is sensitive to C and N abundances, as well as to the O excess, $(O - C)$. Figure 9 shows that at any temperature, the CN abundance increases as we move along the sequence GS98, AAG21, and MBS22. How can we explain these findings? Clearly, the chemistry of CN is the result of solving the equation of state by integrating a complex system of differential equations. However, we can glean an insightful answer from the work of Scalo (1974), who developed a simplified but valid analytic treatment of CN chemistry and demonstrated that in stars with C/O < 1, CN abundance scales roughly as

$$CN \; \propto \; \frac{\sqrt{N}\,C}{O - C} \equiv \tilde{A}_{CN}. \qquad (9)$$

We verified that $\log(\tilde{A}_{CN,GS98}) = 3.942$, $\log(\tilde{A}_{CN,AAG21}) = 4.071$, $\log(\tilde{A}_{CN,MBS22}) = 4.196$ using the solar abundances of the three solar compositions, which is consistent with the increasing order of the CN abundances from the full ÆSOPUS computation.

At lower temperatures, $\log(T/K) \lesssim 3.4$, the H_2O bump contributes the most to the opacity, the abundance of which is primarily determined by the oxygen excess over carbon, $(O - C)_\odot$ (see discussion in Section 4.1). The highest H_2O abundance, as expected, corresponds to GS98, which has the highest $(O - C)_\odot$, whereas MBS22 and AAG21 have similar H_2O concentrations reflecting close oxygen excess values (see Table 3).

In light of these chemistry arguments, we now have the proper tools to interpret the opacity difference maps shown in the bottom panels of Figure 8. We notice that the greatest opacity differences are observed between GS98 and MBS22 (left panel). On the one hand, the higher CN abundance of MBS22 compared to GS98 may contribute to an increase in opacity by about the same amount (red region). On the other hand, the smaller $(O - C)_\odot$ of MBS22 compared to GS98 (by about 0.18 dex; see Table 3) explains the lower MBS22 opacity where H_2O prevails (blue region). When AAG21 and MBS22 are compared (right panel), the opacity differences are smaller and do not exceed 0.1 dex. The Rosseland mean opacities for the MBS22 solar mixture are only slightly lower than those for the AAG21 solar mixture (blue region), reflecting the similar concentrations of H^-, CN, and H_2O.

5. Preliminary Evolutionary Tests

While a detailed analysis of the impact of low-temperature opacities on stellar structure and evolution is beyond the scope of this paper, we discuss two illustrative cases here, namely, the predicted location in the H-R diagram of the Hayashi tracks drawn by low-mass stars as they evolve through the red giant branch (RGB) and thermally pulsing AGB (TP-AGB) phases. We used the COLIBRI code to perform numerical integrations
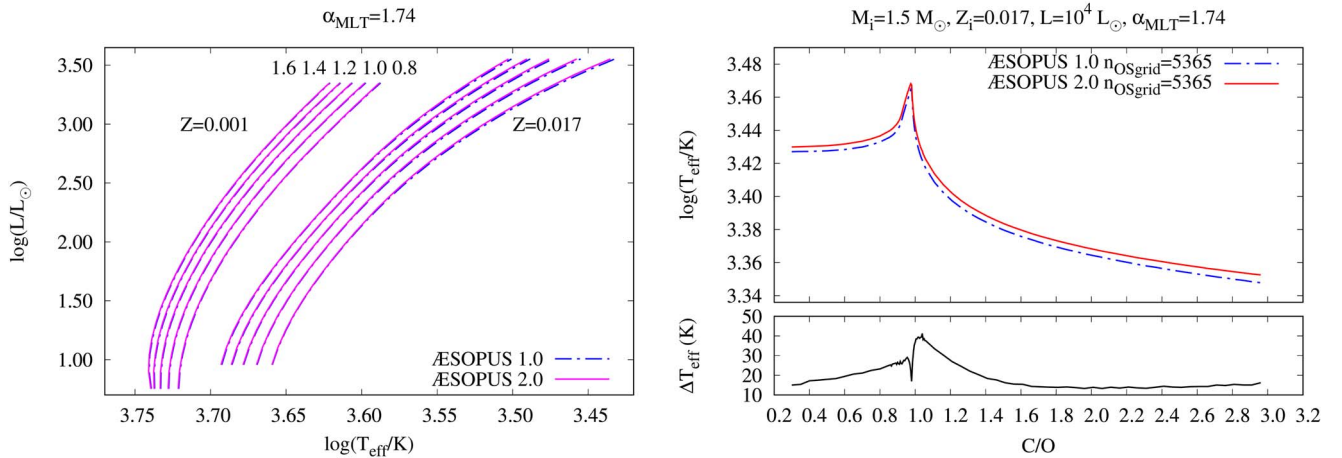
Figure 10. Differences in effective temperature caused by using either ÆSOPUS 1.0 (blue lines) or ÆSOPUS 2.0 (magenta lines) opacities in red giant models. The reference solar composition is MBS22. Left panel: RGB tracks predicted on the H-R diagram with $Z = 0.001$ and 0.017 and M_i ranging from 0.8 to 1.6 $M_\odot$ (with a mass step of 0.2 $M_\odot$). Right panel: predicted effective temperature as a function of increasing photospheric C/O in a TP-AGB star (top) and difference ΔT_{eff} between the two ÆSOPUS versions (bottom). The selected stellar parameters and frequency grid size are indicated. See text for more details.

of a complete envelope model that extends from the atmosphere down to the surface of the degenerate core (Marigo et al. 2013). The COLIBRI code is an appropriate tool for our preliminary tests because it fully incorporates ÆSOPUS as a subroutine for both equation of state and opacity. The mixing-length parameter is set to $\alpha_{MLT} = 1.74$. The procedure is fully described in Marigo et al. (2013). In this way, we can investigate the differences in effective temperature, T_{eff}, caused by using ÆSOPUS 1.0 or ÆSOPUS 2.0 opacities.

The left panel of Figure 10 depicts a series of RGB tracks with varying initial masses and two metallicity values, $Z = 0.001$ and 0.017. At a given Z, all tracks have the same chemical composition, extracted from PARSEC RGB models with $M_i = 1.0 M_\odot$ after the first dredge-up. The luminosity is calculated using the Boothroyd & Sackmann (1988) core mass–luminosity relation as the core mass increases from 0.20 to $0.46 M_\odot$. As expected, RGB tracks move to higher T_{eff} as stellar mass increases and become more luminous at higher metallicity for the same core mass. We can see that the sequences with ÆSOPUS 2.0 opacities are slightly warmer in T_{eff}, corresponding to an $\approx$3–15 K difference. At these temperatures, the H^- opacity contribution is significant, but the McLaughlin et al. (2017) revision has little effect.

In the right panel of Figure 10, we investigate the effect of the two ÆSOPUS versions on a TP-AGB star of a given luminosity ($L = 10^4 L_\odot$) as the photospheric C/O increases from 0.3 to 3 as a result of a progressive carbon enrichment to the surface. This is intended to simulate the effect of the third dredge-up in a simple way. The behavior of the effective temperature as a function of C/O is well understood, and it reflects the abrupt change in molecular equilibrium that occurs when C/O enters the critical range, $(C/O)_{crit} \lesssim C/O \lesssim 1$ (see Table 3 of this work and Section 4.2 of Marigo & Aringer 2009 for a detailed discussion). In these conditions, the majority of C and O atoms are locked in the stable CO molecule, and the opacity drops dramatically, causing the effective temperature to rise. As C/O exceeds unity and more carbon is injected into the atmosphere, the opacity caused by carbon-bearing species significantly lowers the effective temperature, a well-known property of carbon stars (e.g., Marigo 2002). When the results with ÆSOPUS 1.0 and ÆSOPUS 2.0 are compared, we see that the new opacities produce larger effective temperatures (by

$\approx$10–40 K) across the entire range of C/O considered in the test calculations. At C/O < 1, this should be due to a lower opacity contribution of H_2O, whereas at C/O > 1, several carbon-rich opacity sources contribute to κ_R (e.g., CN, HCN, C_2, C_3, and C_2H_2). We notice that the discrepancies reach a minimum at C/O ≈ 1, where molecular absorption is greatly diminished.

In Section 3.3, we demonstrated that reducing the number of frequency points results in small opacity differences, in the range of 0.02–0.03 dex in $\log(\kappa_R)$, provided the sampling distribution meets the energy requirements of the Helling & Jørgensen (1998) optimization scheme (see Figure 5). What effect do these opacity differences have on stellar models? To answer this question, we revisited the TP-AGB star test at increasing C/O discussed above, as shown in Figure 10 (right plot). This test is particularly appropriate because it covers a relevant range of effective temperatures where molecular absorption is important, as well as a wide range of chemistry configurations.

We ran two sets of models with ÆSOPUS 2.0 opacities, one with $n_{OSgrid} = 5365$ points and the other with $n_{OSgrid} = 1458$ points. The effective temperatures derived from complete model atmospheres are compared in Figure 11. We can see that the differences are tiny, ranging between -4 and 2 K across the entire C/O range. This simple experiment reassures us that even our smallest grid size preserves a high level of precision in the integration of giant stars' external layers. Finally, we warn the reader that a thorough investigation of the impact of the new ÆSOPUS 2.0 opacities requires extensive evolutionary calculations, which will be addressed in subsequent studies.

6. Precomputed Opacity Tables

Using ÆSOPUS 2.0, we generated a large grid of scaled-solar Rosseland mean opacity tables for a variety of initial metallicity values (from $Z = 0$ to 0.5) and underlying solar mixture options. All opacity tables span the temperature range $3.2 \leqslant \log(T) \leqslant 4.5$ and R range $-1.0 \leqslant \log(R) \leqslant 8.0$. Similarly to the OPAL opacity format (Iglesias & Rogers 1996), for each metallicity, we consider 10 potential hydrogen abundance values ($X = 0$, 0.1, 0.2, 0.35, 0.5, 0.7, 0.8, 0.9, 0.95, and 1), but, when necessary, we reduce the number of X
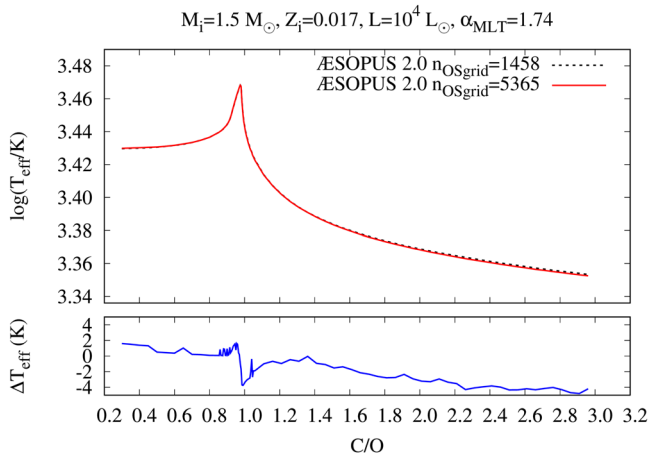
Figure 11. Effective temperature predicted by the integration of a red giant's model atmosphere. The test is designed to assess the sensitivity to the frequency grid size used to compute κ_R. Top panel: effective temperature of a TP-AGB star with $L = 10^4 \, L_\odot$ and increasing photospheric C/O using $n_{OSgrid} = 5365$ (solid line) or 1458 (dotted line). Bottom panel: difference in effective temperature between atmospheric integrations using the two frequency grids. Both frequency distributions are extracted following the Helling & Jørgensen (1998) OS optimization prescriptions.

nodes to comply with the condition that X cannot exceed $1 - Z$. In fact, at each metallicity, $X = 1 - Z$ always represents the maximum hydrogen value of the node sequence. The Rosseland mean opacity tables are available via the repository at http://stev.oapd.inaf.it/aesopus_2.0/tables; a copy of these files have also been deposited to Zenodo: https://doi.org/10.5281/zenodo.7219874.

7. Arbitrary Chemical Mixtures: The Need for a Web Interface

ÆSOPUS can easily generate opacity tables for arbitrary chemical abundance distributions, such as those with varying CNO abundances, suitable for evolutionary models of red and AGB stars and massive rotating stars; various degrees of enhancement in α-elements; C–N, O–Na, and Mg–Al abundance anticorrelations, which are required to properly describe the properties of stars in Galactic globular clusters; and extremely metal-poor or zero-metallicity mixtures suitable for studies of gas opacity in primordial conditions, to name a few. Several applications were discussed in detail in the original paper (Marigo & Aringer 2009) and will not be repeated here.

Because the era of high-resolution and large spectroscopic surveys (e.g., Randich et al. 2013, the Gaia-ESO Large Public Spectroscopic Survey; Zhao et al. 2012, LAMOST; De Silva et al. 2015, GALAH; Majewski et al. 2017, APOGEE; see also Jofré et al. 2019 for a comprehensive review) has been revealing a wide variety of abundance patterns in stars, creating archives of opacity tables for any scenario makes little sense. A profitable way to deal with such abundance data richness is to provide a public web interface where users can personalize their opacity query.

In this perspective and to greatly increase the availability of low-temperature opacities, Marigo & Aringer (2009) created an interactive web interface (http://stev.oapd.inaf.it/aesopus) that allows users to run ÆSOPUS 1.0 based on their specific needs simply by entering the input parameters (T–R grid, reference solar mixture, metallicity, abundance of each chemical species) on the web mask. The interface has now been updated to

include the major revision introduced in ÆSOPUS 2.0 while maintaining the high level of flexibility and quick computational performance that distinguishes our public tool. It is accessible via http://stev.oapd.inaf.it/aesopus_2.0. The previous web interface, corresponding to ÆSOPUS 1.0, is still available at http://stev.oapd.inaf.it/aesopus_1.0.

8. Concluding Remarks

Updated ÆSOPUS low-temperature opacities have been computed for various solar mixtures and made publicly available for primary use in stellar models. The tables can be obtained through a static repository at http://stev.oapd.inaf.it/aesopus_2.0/tables; a copy of these files has also been deposited to Zenodo: https://doi.org/10.5281/zenodo.7219874. The major changes are improved input physics and numerical procedures to speed up computational effort while maintaining high accuracy. Among the updates are recommended line lists for 80 absorbing molecular species from the ExoMol and HITRAN databases, new data for H^- photodetachment bound–free absorption, and revised CIA. The most recent solar mixtures from AAG21 and MBS22 are added. The ÆSOPUS web interface has been renovated to integrate all of the changes introduced in this work. It is available at http://stev.oapd.inaf.it/aesopus_2.0. User feedback is encouraged.

This significant update in the ÆSOPUS code and related deliverables is only the first step in a major revision and expansion of our tools for dealing with opacity tables. Future works will address opacities in the high-temperature regime, opacities of heavy elements such as lanthanides and actinides, a systematic update of partition functions, and novel interpolation schemes. Furthermore, any opacity revisions will be incorporated and tested in the PARSEC (Bressan et al. 2012; Costa et al. 2019) and COLIBRI (Marigo et al. 2013) stellar evolutionary codes.

Finally, we conclude with a few thoughts on the needs we believe are critical to improving the opacities for the stellar community. The availability of accurate and comprehensive energy levels, line positions, oscillator strengths, and cross sections for significant absorbing species (atoms, ions, anions, molecules, and transitory dipoles produced in collisions) is required for robust and reliable integration of Rosseland mean opacities. There has been a lot of work done in recent years to build extensive molecular line lists, such as the coordinated project ExoMol, which is primarily designed for exoplanets. ExoMol also provides a suite of user-friendly tools for computing partition functions and opacity cross sections. The included energy levels are usually complete enough to cover the typical temperatures of the stellar atmospheric layers where molecules can form.

For cool stars with C/O < 1, the situation with the line lists is quite favorable. For example, we can now rely on previously unavailable data for molecules such as AlH, NaH, and CaOH, which are essential for modeling the atmospheres of M dwarfs. Still, further effort needs to made to improve stellar opacities. Pressure broadening should be taken into account for both M and brown dwarfs. The modeling is complex, and it is partly hampered by poor knowledge of the broadening parameters for major collision broadeners, such as H_2 and He, at relatively high temperatures.

Transition metal-bearing diatomic molecules are important opacity sources at near-infrared and visible wavelengths. We have line lists for several species, including TiO, VO, FeH,

ScH, TiH, CrH, NiH, ZrO, and YO, but there are many other candidates that lack data (e.g., MnH, FeO, TiZr, and ZrV). The chemistry of carbon stars with C/O > 1 is more complex. For some molecules, such as C_3, which is an important opacity source in cool carbon stars with a high C/O ratio, we still rely on old line lists (Jorgensen et al. 1989) that deserve to be improved. In fact, it is well known that the existing computed opacities do not accurately reproduce the observed spectral features of this species (Aringer et al. 2019). Furthermore, there could be other significant opacity sources in carbon stars for which we have no data at all (e.g., C_2H). The cross sections of some bound–free and free–free processes, such as those of anions of atoms and molecules, are estimated from early studies carried out many decades ago (see Table 1). A modern revision would undoubtedly be beneficial.

ORCID iDs

Paola Marigo ⓘ https://orcid.org/0000-0002-9137-0773
Bernhard Aringer ⓘ https://orcid.org/0000-0001-9848-5410
Léo Girardi ⓘ https://orcid.org/0000-0002-6301-3269
Alessandro Bressan ⓘ https://orcid.org/0000-0002-7922-8440

References

Abel, M., Frommhold, L., Li, X., & Hunt, K. L. C. 2011, JPCA, 115, 6805
Abel, M., Frommhold, L., Li, X., & Hunt, K. L. C. 2012, JChPh, 136, 044319
Adam, A. Y., Yachmenev, A., Yurchenko, S. N., & Jensen, P. 2019, JPCA, 123, 4755
Al Derzi, A. R., Furtenbacher, T., Tennyson, J., Yurchenko, S. N., & Csaszar, A. G. 2015, JQSRT, 161, 117
Alexander, D. R., & Ferguson, J. W. 1994, ApJ, 437, 879
Althaus, L. G., García-Berro, E., Renedo, I., et al. 2010, ApJ, 719, 612
Amaral, P. H. R., Diniz, L. G., Jones, K. A., et al. 2019, ApJ, 878, 95
Anders, E., & Grevesse, N. 1989, GeCoA, 53, 197
Aringer, B., Marigo, P., Nowotny, W., et al. 2019, MNRAS, 487, 2133
Asplund, M., Amarsi, A. M., Grevesse, N., et al. 2021, A&A, 653, A141
Asplund, M., Grevesse, N., Sauval, A. J., & Scott, P. 2009, ARA&A, 47, 481
Azzam, A. A. A., Tennyson, J., Yurchenko, S. N., & Naumenko, O. V. 2016, MNRAS, 460, 4063
Barber, R. J., Tennyson, J., Harris, G. J., & Tolchenov, R. N. 2006, MNRAS, 368, 1087
Barklem, P. S., & Collet, R. 2016, A&A, 588, A96
Barton, E. J., Chiu, C., Golpayegani, S., et al. 2014, MNRAS, 442, 1821
Bell, K. L., & Berrington, K. A. 1987, JPhB, 20, 801
Bell, K. L., Hibbert, A., & Berrington, K. A. 1988, JPhB, 21, 2319
Bernath, P. F. 2020, JQSRT, 240, 106687
Bittner, D. M., & Bernath, P. F. 2018, ApJS, 235, 8
Boothroyd, A. I., & Sackmann, I.-J. 1988, ApJ, 328, 641
Borysow, A., Jørgensen, U. G., & Zheng, C. 1997, A&A, 324, 185
Bowesman, C. A., Shuai, M., Yurchenko, S. N., & Tennyson, J. 2021, MNRAS, 508, 3181
Bressan, A., Marigo, P., Girardi, L., et al. 2012, MNRAS, 427, 127
Brooke, J. S. A., Bernath, P. F., & Western, C. M. 2015, JChPh, 143, 026101
Brooke, J. S. A., Bernath, P. F., Western, C. M., et al. 2016, JQSRT, 168, 142
Burrows, A., Dulick, M., Bauschlicher, C. W., Jr., et al. 2005, ApJ, 624, 988
Caffau, E., Ludwig, H.-G., Steffen, M., Freytag, B., & Bonifacio, P. 2011, SoPh, 268, 255

Chandrasekhar, S., & Breen, F. H. 1946, ApJ, 104, 430
Chubb, K. L., Rocchetto, M., Yurchenko, S. N., et al. 2021, A&A, 646, A21
Chubb, K. L., Tennyson, J., & Yurchenko, S. N. 2020, MNRAS, 493, 1531
Coles, P. A., Yurchenko, S. N., & Tennyson, J. 2019, MNRAS, 490, 4638
Coppola, C. M., Lodi, L., & Tennyson, J. 2011, MNRAS, 415, 487
Costa, G., Girardi, L., Bressan, A., et al. 2019, MNRAS, 485, 4641
Coxon, J. A., & Hajigeorgiou, P. G. 2015, JQSRT, 151, 133
Dalgarno, A. 1962, Spectral Reflectivity of the Earth Atmosphere III: The Scattering of light by Atomic Systems, GCA Tech Rep., 62-28-A, Geophys. Corp. of America
Dalgarno, A., & Williams, D. A. 1962, ApJ, 136, 690
Darby-Lewis, D., Tennyson, J., Lawson, K. D., et al. 2018, JPhB, 51, 185701
De Silva, G. M., Freeman, K. C., Bland-Hawthorn, J., et al. 2015, MNRAS, 449, 2604
Dulick, M., Bauschlicher, C. W., Jr., Burrows, A., et al. 2003, ApJ, 594, 651
Ferguson, J. W., Alexander, D. R., Allard, F., et al. 2005, ApJ, 623, 585
Ferland, G. 2000, University of Kentucky Internal Report
Fernando, A. M., Bernath, P. F., Hodges, J. N., & Masseron, T. 2018, JQSRT, 217, 29
Ferrarotti, A. S., & Gail, H.-P. 2006, A&A, 447, 553
Frohman, D. J., Bernath, P. F., & Brooke, J. S. A. 2016, JQSRT, 169, 104
Frommhold, L. 1994, Collision-induced Absorption in Gases (Cambridge: Cambridge Univ. Press)
Gallagher, A. J., Bergemann, M., Collet, R., et al. 2020, A&A, 634, A55
Gavrila, M. 1967, PhRv, 163, 147
Gil-Pons, P., Doherty, C. L., Gutierrez, J. L., et al. 2018, PASA, 35, e038
Gingerich, O. 1964, SAOSR, 167, 17
Gordon, I. E., Rothman, L. S., Hargreaves, R. J., et al. 2022, JQSRT, 277, 107949
Gordon, I. E., Rothman, L. S., Hill, C., et al. 2017, JQSRT, 203, 3
Gorman, M. N., Yurchenko, S. N., & Tennyson, J. 2019, MNRAS, 490, 1652
Grevesse, N., Asplund, M., & Sauval, A. J. 2007, SSRv, 130, 105
Grevesse, N., & Noels, A. 1993, in Origin and Evolution of the Elements, ed. N. Prantzos, E. Vangioni-Flam, & M. Casse (Cambridge: Cambridge Univ. Press)
Grevesse, N., & Sauval, A. J. 1998, SSRv, 85, 161
Grimm, S. L., Malik, M., Kitzmann, D., et al. 2021, ApJS, 253, 30
Gustafsson, M., & Frommhold, L. 2001, ApJ, 546, 1168
Gustafsson, M., & Frommhold, L. 2003, A&A, 400, 1161
Harris, G. J., Lynas-Gray, A. E., Miller, S., & Tennyson, J. 2004, ApJ, 600, 1025
Harris, G. J., Tennyson, J., Kaminsky, B. M., Pavlenko, Y. V., & Jones, H. R. A. 2006, MNRAS, 367, 400
Helling, C., & Jørgensen, U. G. 1998, A&A, 337, 477
Henry, R. J. W. 1970, ApJ, 161, 1153
Hodges, J. N., & Bernath, P. F. 2017, ApJ, 840, 81
Holweger, H. 2001, in AIP Conf. Ser. 598, Solar and Galactic Composition (Joint SOHO/ACE workshop), ed. R. F. Wimmer-Schweingruber (Melville, NY: AIP), 23
Hou, S., & Bernath, P. F. 2017, JQSRT, 203, 511
Hou, S., & Bernath, P. F. 2018, JQSRT, 210, 44
Hunger, K., & van Blerkom, D. 1967, ZAp, 66, 185
Iglesias, C. A., & Rogers, F. J. 1996, ApJ, 464, 943
Jofré, P., Heiter, U., & Soubiran, C. 2019, ARA&A, 57, 571
John, T. L. 1975, MNRAS, 172, 305
John, T. L. 1988, A&A, 193, 189
John, T. L. 1994, MNRAS, 269, 871
John, T. L. 1996, MNRAS, 279, 859
John, T. L., Morgan, D. J., & Wickramasinghe, N. C. 1975, MNRAS, 170, 1
Jørgensen, U. G. 1997, in IAU Symp. 178, Molecules in Astrophysics: Probes & Processes, ed. E. van Dishoeck (Dordrecht: Kluwer), 441
Jorgensen, U. G., Almlof, J., & Siegbahn, P. E. M. 1989, ApJ, 343, 554
Jørgensen, U. G., Hammer, D., Borysow, A., & Falkesgaard, J. 2000, A&A, 361, 283
Jørgensen, U. G., & Larsson, M. 1990, A&A, 238, 424
Karakas, A. I., & Lugaro, M. 2016, ApJ, 825, 26
Karman, T., Gordon, I. E., van der Avoird, A., et al. 2019, Icar, 328, 160
Karzas, W. J., & Latter, R. 1961, ApJS, 6, 167
Kurucz, R. L. 1970, SAO Special Report, 309, Smithsonian Institution
Lampel, J., Pöhler, D., Polyansky, O. L., et al. 2017, ACP, 17, 1271
Langleben, J., Tennyson, J., Yurchenko, S. N., & Bernath, P. 2019, MNRAS, 488, 2332
Lebedev, V. S., Presnyakov, L. P., & Sobel'man, I. I. 2003, PhyU, 46, A02
Lederer, M. T., & Aringer, B. 2009, A&A, 494, 403
Li, G., Gordon, I. E., Bernath, P. F., & Rothman, L. S. 2011, JQSRT, 112, 1543

Li, G., Gordon, I. E., Le Roy, R. J., et al. 2013, JQSRT, 121, 78
Li, G., Gordon, I. E., Rothman, L. S., et al. 2015, ApJS, 216, 15
Li, H. Y., Tennyson, J., & Yurchenko, S. N. 2019, MNRAS, 486, 2351
Lodders, K. 2003, ApJ, 591, 1220
Lodi, L., Yurchenko, S. N., & Tennyson, J. 2015, MolPh, 113, 1998
Magg, E., Bergemann, M., Serenelli, A., et al. 2022, A&A, 661, A140
Majewski, S. R., Schiavon, R. P., Frinchaboy, P. M., et al. 2017, AJ, 154, 94
Mant, B. P., Yachmenev, A., Tennyson, J., & Yurchenko, S. N. 2018, MNRAS, 478, 3220
Marigo, P. 2002, A&A, 387, 507
Marigo, P., & Aringer, B. 2009, A&A, 508, 1539
Marigo, P., Bressan, A., Nanni, A., Girardi, L., & Pumo, M. L. 2013, MNRAS, 434, 488
Masseron, T., Plez, B., Van Eck, S., et al. 2014, A&A, 571, A47
Mayer, M., & Duschl, W. J. 2005, MNRAS, 358, 614
McKemmish, L. K., Masseron, T., Hoeijmakers, H. J., et al. 2019, MNRAS, 488, 2836
McKemmish, L. K., Syme, A.-M., Borsovszky, J., et al. 2020, MNRAS, 497, 1081
McKemmish, L. K., Yurchenko, S. N., & Tennyson, J. 2016, MNRAS, 463, 771
McLaughlin, B. M., Stancil, P. C., Sadeghpour, H. R., & Forrey, R. C. 2017, JPhB, 50, 114001
Mitev, G. B., Taylor, S., Tennyson, J., et al. 2022, MNRAS, 511, 2349
Mizus, I. I., Alijah, A., Zobov, N. F., et al. 2017, MNRAS, 468, 1717
Mucciarelli, A. 2011, A&A, 528, A44
Owens, A., Conway, E. K., Tennyson, J., & Yurchenko, S. N. 2020, MNRAS, 495, 1927
Owens, A., Dooley, S., McLaughlin, L., et al. 2022, MNRAS, 511, 5448
Owens, A., Tennyson, J., & Yurchenko, S. N. 2021, MNRAS, 502, 1128
Owens, A., Yachmenev, A., Thiel, W., Tennyson, J., & Yurchenko, S. N. 2017, MNRAS, 471, 5025
Owens, A., Yachmenev, A., Thiel, W., et al. 2018, MNRAS, 479, 3002
Partridge, H., & Schwenke, D. W. 1997, JChP, 106, 4618
Patrascu, A. T., Yurchenko, S. N., & Tennyson, J. 2015, MNRAS, 449, 3613
Paulose, G., Barton, E. J., Yurchenko, S. N., & Tennyson, J. 2015, MNRAS, 454, 1931
Paxton, B., Bildsten, L., Dotter, A., et al. 2011, ApJS, 192, 3
Peach, G. 1970, MmRAS, 73, 1
Plez, B. 2012, Turbospectrum: Code for Spectral Synthesis, Astrophysics Source Code Library, ascl:1205.004
Plez, B., Smith, V. V., & Lambert, D. L. 1993, ApJ, 418, 812
Polyansky, O. L., Kyuberis, A. A., Zobov, N. F., et al. 2018, MNRAS, 480, 2597
Prajapat, L., Jagoda, P., Lodi, L., et al. 2017, MNRAS, 472, 3648
Qin, Z., Bai, T., & Liu, L. 2021, JQSRT, 258, 107352
Qu, Q., Yurchenko, S. N., & Tennyson, J. 2021, MNRAS, 504, 5768
Ram, R. S., Brooke, J. S. A., Western, C. M., & Bernath, P. F. 2014, JQSRT, 138, 107
Ramsbottom, C. A., & Bell, K. L. 1996, PhyS, 54, 250
Ramsbottom, C. A., Bell, K. L., & Berrington, K. A. 1992, JPhB, 25, 1443
Randich, S., Gilmore, G. & Gaia-ESO Consortium 2013, Msngr, 154, 47

Rivlin, T., Lodi, L., Yurchenko, S. N., Tennyson, J., & Le Roy, R. J. 2015, MNRAS, 451, 634
Roueff, E., Abgrall, H., Czachorowski, P., et al. 2019, A&A, 630, A58
Scalo, J. M. 1974, ApJ, 194, 361
Seaton, M. J. 1995, in AIP Conf. Proc. 322, Atomic Processes in Plasmas (Melville, NY: AIP), 117
Seaton, M. J., Yan, Y., Mihalas, D., & Pradhan, A. K. 1994, MNRAS, 266, 805
Semenov, D., Henning, T., Helling, C., Ilgner, M., & Sedlmayr, E. 2003, A&A, 410, 611
Serenelli, A. M., Basu, S., Ferguson, J. W., & Asplund, M. 2009, ApJL, 705, L123
Sharp, C. M., & Burrows, A. 2007, ApJS, 168, 140
Smirnov, A. N., Solomonik, V. G., Yurchenko, S. N., & Tennyson, J. 2019, PCCP, 21, 22794
Somogyi, W., Yurchenko, S. N., & Yachmenev, A. 2021, JChP, 155, 214303
Sousa-Silva, C., Al-Refaie, A. F., Tennyson, J., & Yurchenko, S. N. 2014, MNRAS, 446, 2337
Syme, A.-M., & McKemmish, L. K. 2021, MNRAS, 505, 4383
Takei, Y., & Shigeyama, T. 2020, PASJ, 72, 67
Tennyson, J., & Yurchenko, S. N. 2012, MNRAS, 425, 21
Trabucchi, M., Wood, P. R., Mowlavi, N., et al. 2021, MNRAS, 500, 1575
Underwood, D. S., Tennyson, J., Yurchenko, S. N., et al. 2016, MNRAS, 459, 3890
Upadhyay, A., Conway, E. K., Tennyson, J., & Yurchenko, S. N. 2018, MNRAS, 477, 1520
Van Eck, S., Neyskens, P., Jorissen, A., et al. 2017, A&A, 601, A10
Vanture, A. D., & Wallerstein, G. 2002, ApJ, 564, 395
Ventura, P., Karakas, A., Dell'Agli, F., García-Hernández, D. A., & Guzman-Ramirez, L. 2018, MNRAS, 475, 2282
Wishart, A. W. 1979, MNRAS, 187, 59P
Yorke, L., Yurchenko, S. N., Lodi, L., & Tennyson, J. 2014, MNRAS, 445, 1383
Yousefi, M., Bernath, P. F., Hodges, J., & Masseron, T. 2018, JQSRT, 217, 416
Yurchenko, S. N., Al-Refaie, A. F., & Tennyson, J. 2018a, A&A, 614, A131
Yurchenko, S. N., Amundsen, D. S., Tennyson, J., & Waldmann, I. P. 2017a, A&A, 605, A95
Yurchenko, S. N., Blissett, A., Asari, U., et al. 2016, MNRAS, 456, 4524
Yurchenko, S. N., Bond, W., Gorman, M. N., et al. 2018b, MNRAS, 478, 270
Yurchenko, S. N., Mellor, T. M., Freedman, R. S., & Tennyson, J. 2020a, MNRAS, 496, 5282
Yurchenko, S. N., Sinden, F., Lodi, L., et al. 2017b, MNRAS, 473, 5324
Yurchenko, S. N., Szabó, I., Pyatenko, E., & Tennyson, J. 2018c, MNRAS, 480, 3397
Yurchenko, S. N., & Tennyson, J. 2014, MNRAS, 440, 1649
Yurchenko, S. N., Tennyson, J., Miller, S., et al. 2020b, MNRAS, 497, 2340
Yurchenko, S. N., Tennyson, J., Syme, A.-M., et al. 2022, MNRAS, 510, 903
Yurchenko, S. N., Williams, H., Leyland, P. C., Lodi, L., & Tennyson, J. 2018d, MNRAS, 479, 1401
Zhao, G., Zhao, Y.-H., Chu, Y.-Q., Jing, Y.-P., & Deng, L.-C. 2012, RAA, 12, 723